Optical frequency comb generation in gas-filled hollow core photonic crystal fibres

2009 J. Opt. A: Pure Appl. Opt. 11 103002

(http://iopscience.iop.org/1464-4258/11/10/103002)

J. Opt. A: Pure Appl. Opt. **11** (2009) 103002 (16pp) doi:10.1088/1464-4258/11/10/103002

REVIEW ARTICLE

Optical frequency comb generation in gas-filled hollow core photonic crystal fibres

F Couny and F Benabid

Centre for Photonics and Photonic Materials, University of Bath, Bath BA2 7AY, UK

E-mail: f.y.m.couny@bath.ac.uk

Received 18 February 2009, accepted for publication 2 July 2009
Published 6 August 2009
Online at stacks.iop.org/JOptA/11/103002

Abstract
The efficiency of gas-based nonlinear processes is often limited by the diffraction of the pump laser as it propagates through the nonlinear medium. As a consequence, phenomena with strong nonlinear response requirements, such as high harmonic generation or Raman sideband generation, lack the required laser–matter interaction to fulfil their potential. Indeed, the conversion efficiency of these techniques is usually low and the experimental set-up cumbersome. The advent of hollow core photonic crystal fibre technology drafts new territories for nonlinear optics, and in particular offers new alternatives for sub-femtosecond pulse generation. The air-guiding fibre combines unprecedented laser confinement over long interaction lengths and, when filled with an adequate nonlinear gas, offers improved conversion efficiency and up to a million-fold reduction of the pump power threshold. This paper presents a review of the types of hollow core PCF available for nonlinear applications and the results obtained for efficient Raman conversion in H_2-filled hollow core PCF that led to the observation of a multi-octave frequency comb spanning from ∼325 to ∼2300 nm using a single pump laser with relatively low power. The generated ultra-broad spectrum creates a simple route towards a compact source of attosecond pulses.

Keywords: Raman laser, hollow core photonic crystal fibre, stimulated Raman scattering, gas–laser cavity device, fibre Bragg grating

(Some figures in this article are in colour only in the electronic version)

1. Introduction

The efficient excitation of extreme nonlinearities has become a necessary prerequisite to push further the boundaries of quantum and nonlinear optical effects. The emerging atto-science, which aims at studying and controlling ultra-fast physical and chemical processes, is a perfect embodiment of such an endeavour. Through the generation of a phase-locked optical frequency comb reaching the soft x-ray region of the optical spectrum, the high harmonic generation (HHG) method already demonstrated attosecond (10^{-18} s) pulse generation using femtosecond (10^{-15} s) lasers [1, 2]. However, the technique relies on the excitation of a noble gas by an ultra-short pulsed laser with power of the order of a petawatt (10^{15} W) per centimetre square. Additional limitations due to the low photon conversion efficiency and engineering difficulties of the process mean that new routes are being explored. One of them consists of coherently driving a Raman-active medium, in general in its gaseous form, by the use of two high power lasers [3, 4]. The resulting Raman sidebands, spanning the UV and near-IR, have been shown to exhibit similar properties to those obtained via HHG, though with a much lower nonlinear threshold and higher quantum conversion. Both methods strongly depend on the efficiency of the laser–matter interaction, often restricted by laser beam diffraction, which means that multiple high power

lasers have to be used in an often cumbersome set-up. These limitations could be lifted by the recent development of hollow core optical fibres capable of confining together gases and light in micrometre-scale areas over potentially hundreds of metres. These fibres create a new paradigm in gas–laser interaction, where extreme nonlinearities can be achieved with unprecedented low light power levels in compact, all-fibre systems [5].

Section 2 of this review presents the state-of-the-art of the hollow core fibre technology and the key steps that led to the realization of a photonic microcell, based on a gas-filled hollow core fibre. Section 3 of the review describes the many milestones achieved in stimulated Raman scattering in these microcells, including a dramatic reduction of the required power for Raman amplification, leading to the realization of the first fibre-based continuous-wave (CW) Raman gas laser; and a way to control the transient regime of amplification using nanosecond laser pump pulses, crucial to the realization of a phase-locked frequency comb. Section 4 of the review presents the experimental results obtained in the generation of ultra-broad frequency combs spanning from the UV to the IR with ultra-low power threshold and with a conversion efficiency of ∼50% in a H_2-filled hollow core fibre. The potential combination of the CW Raman laser and the frequency comb generator obtained using these fibres offers a new direction for femtosecond pulse compression and efficient attosecond pulse generation using a single, low power CW pump laser source.

2. Hollow core photonic crystal fibre

For nonlinear processes such as HHG or Raman scattering to be efficient, a large number of photons are required to interact with the nonlinear medium over a distance as long as possible and with a transverse confinement as tight as possible. In a free-space propagation experiment, this is generally achieved by focusing the laser beam onto an effective area limited by the minimum beam waist, over a length that is typically limited to twice the Rayleigh length. This therefore restricts drastically the efficiency of the process and can also generate unwanted high power nonlinearity [6].

In order to circumvent this problem, two routes can be followed: either increase the length over which the photons interact with the nonlinear medium or increase the number of photons present inside it (i.e. increase the laser intensity). Whilst the use of hollow silica capillaries filled with the required nonlinear material modestly addresses the former solution by enhancing the effective length by a factor of 10–100, the power required to achieve nonlinearity is only reduced by a few orders of magnitude compared to free space [7]. Increasing the number of photons inside the nonlinear medium proved a more efficient solution and was successfully investigated experimentally by placing the medium inside a high finesse cavity and led, for example, to the realization of the first CW Raman laser [8, 9]. However, the method is limited by the bandwidth of the cavity mirrors as well as the electronic control of the cavity resonance to the nonlinear frequencies.

The low attenuation achieved in hollow core photonic crystal fibres (HC-PCF) effectively lifts the free-space diffraction limit so that light can be guided over potentially kilometre length in a micrometre-scale effective area, yielding an efficiency up to 10^6 times higher than free space and without the limitations of the high finesse cavity technique [10]. A HC-PCF consists of a micrometre-scale air hole surrounded by a photonic crystal cladding formed by hundreds of capillaries running along the length of the fibre that act as a photonic barrier so that the light is tightly confined inside the hollow core defect. The key benefit of a gas-filled HC-PCF is that it guides predominantly in its hollow core, thus reducing any detrimental nonlinear effects due to silica in favour of an enhancement of the nonlinear properties of the gas phase medium. The first demonstrations of the outstanding guidance properties of HC-PCF came with the generation of stimulated Raman scattering in H_2-filled HC-PCF [10, 11]. This seminal work served as a springboard to the Raman scattering experiments presented in section 3, and to the demonstration of multi-octave frequency comb generation presented in section 4. Since then, a number of breakthroughs have also been demonstrated in various areas of photonics and nonlinear optics such as high power soliton delivery [12], electromagnetically induced transparency and saturable absorption in both molecular systems [13–16] and atomic vapours [17, 18].

The following section presents the two main types of HC-PCF through which low loss guidance is achieved. Although both fibres rely on a photonic crystal cladding to achieve low loss guidance, their light trapping mechanism differs drastically. This leads to dramatically different optical properties that can be individually tailored to suit a particular application.

2.1. Out-of-plane photonic bandgap

The idea of a hollow core photonic crystal fibre emerged from the suggestion that efficient air-core guidance in fibre could be achieved by adding a photonic crystal cladding around the core to confine the light inside it by means of an out-of-plane photonic bandgap [19]. Inside such a structure (e.g. figure 1(A)), the dielectric function n of the cladding structure and the free-space wavenumber k are linked to the axial wavenumber component β, also called the propagation constant, through the Maxwell–Helmholtz equation:

$$(\nabla^2 + k^2 n^2)h + \nabla(\ln n^2) \times (\nabla \times h) = \beta^2 h \qquad (1)$$

where h is the transverse component of the magnetic field. In the case where light is propagating out of the periodic plane of the photonic crystal [20], Birks *et al* [21] formally identified specific spectral regions for which there exist no solution to equation (1), corresponding to the total exclusion of light from the inside of the structure. The usual way to represent these photonic 'bandgaps' (PBG) is to plot the density of photonic states (DOPS) of the structure, i.e. the number of electromagnetic modes per unit cell and per unit length [22], as a function of the dimensionless normalized parameter $k\Lambda$, where Λ is the pitch of the structure and of the effective

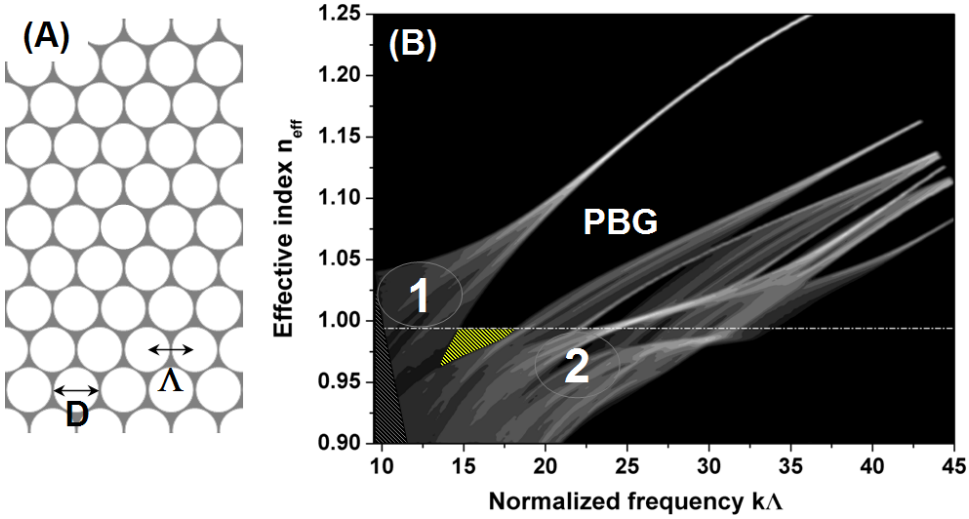

Figure 1. (A) Example of the photonic crystal cladding structure based on a triangular lattice of holes of diameter D and pitch Λ. (B) Calculated density of the photonic state plot for a structure with an air-filling fraction of 91.9% (from [25]). Regions of high density of states are indicated in white, while black represents zero density of state. The bandgap region extending below the air line $n_{\text{eff}} = 1$ is highlighted as a shaded area.

index n_{eff} (figure 1(B)). The cladding modes supported by the photonic structure add up to form bands of high DOPS (bright regions 1 and 2 in figure 1(B)) surrounding 'finger'-shaped photonic bandgap regions (PBG in figure 1(B)). When a PBG region extends below the air line, air guidance becomes possible. Fortunately, the refractive indices of pure silica and air create such a favourable concurrence and an air-guiding PBG fibre can be realized with a micrometre-scale lattice pitch Λ for guidance in the visible and near-infrared ($k\Lambda < 20$).

Very much like the electronic bandgap formation in the atomic structure of a solid crystal, the formation of a photonic bandgap can be said to arise from the various resonators present in the photonic cladding. In analogy to the tight binding model of solid state physics, it was shown theoretically and experimentally that, although the topological structure of the air–silica HC-PCF cladding is complex, a photonic equivalent of the tight binding model could be developed thanks to the sufficiently few resonators involved in forming the cladding modes' spectrum in the vicinity of the bandgap [23]. This point of view stemmed from previous work that considered alternative and more intuitive models to explain the formation of PBG inside photonic crystal structures [24, 25]. The identification of the resonators involved in the triangular lattice of an HC-PCF (figure 1(A)) was carried out by examining the field profiles of the most representative cladding modes. Figure 2 shows the intensity profile of the modes that form the boundaries of the PBG. The mode forming the upper edge is predominantly in the interstitial apices of the cladding, whilst the bottom edge is formed by two modes of different symmetry, one being guided predominantly in the air holes of the cladding lattice, the other guided predominantly within and close to the silica struts which join neighbouring apices. Experimental identification of these modes can be made through the analysis of the Fresnel diffraction pattern of such modes at the output of the fibre [23]. As shown in figures 2(C)–(E), the key features of their theoretical Fresnel profile have been observed experimentally at the expected wavelength. This conceptual framework provides a simple and intuitive understanding of how PBG forms and has allowed the optimization of both the PBG bandwidth and the attenuation of the fibre through increasing both the air-filling fraction of the cladding structure and the aspect ratio between apex size and strut thickness.

2.2. Low loss air-core guidance

The key conclusion to emerge from Birks *et al* [21] was that no light could penetrate inside a PBG so long as the conditions on $k\Lambda$ and n_{eff} are satisfied. As a result, if a defect is introduced in the photonic crystal such that it breaks the transverse periodicity of the structure, light could effectively become trapped inside it. In the case of HC-PCF, the defect is introduced in the centre of the photonic crystal cladding by removing one or several capillaries during fibre fabrication, creating cores of the order of 10 μm in diameter (figures 3(A) and (B)). Remarkably, the refractive index of this core defect is less critical than for total internal reflection so that guidance can actually be achieved in air or liquid with refractive indices lower than that of the cladding material (e.g. silica). Indeed, if one or more bandgaps cross the vacuum dispersion line (air line, $k = \beta$) and if the core shape accommodates modes within the range of propagation constant of the PBG, optical guidance in air is achieved with low attenuation over a frequency span set by the PBG and limited on either sides by the coupling of these core modes with the continuum of cladding modes. Figure 3(C) shows the spatial profiles of air-guided lowest-order 'fundamental' mode and higher-order modes for the case of a core was formed by seven missing unit cells. The optical wavelength range over which guidance is achieved can be easily chosen by fabricating the fibre at the correct cladding pitch Λ.

The resulting fundamental mode has typically >99% of its intensity residing in the air [26]. Consequently, one could expect the attenuation of the fibre to be ultimately limited by the Rayleigh scattering of air, well below the

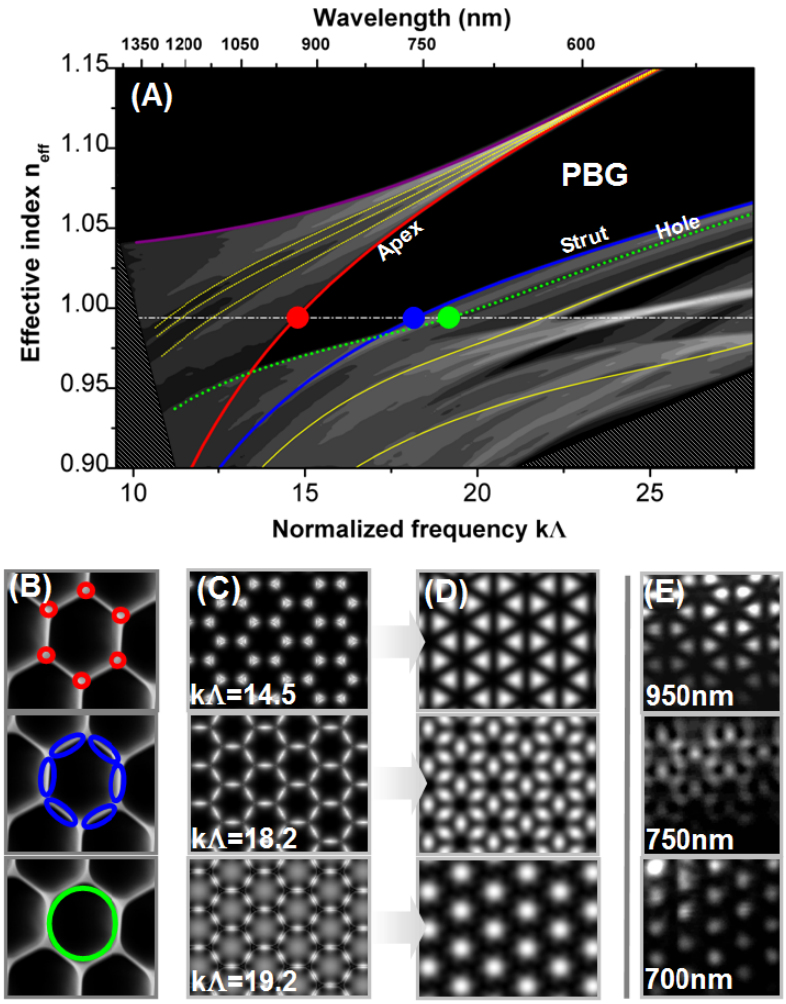

Figure 2. (A) Detail of the calculated density of state plot presented in figure 1 around the photonic bandgap region falling below the vacuum line. The upper X axis shows the corresponding wavelength for a hollow core PCF guiding around 800 nm ($\Lambda = 2.15\ \mu$m). The trajectory of the cladding modes on the edges of the bandgap are represented in red for the interstitial apices mode, blue for the silica strut mode and in green for the air hole mode. (B) Detail of the three resonators identified in the triangular structure. (C) Their calculated near-fields, at a position indicated by the dots in (A). (D) The corresponding calculated Fresnel pattern. (E) Experimental observation of the Fresnel evolution of the cladding modes at wavelengths corresponding to the edges of the bandgap, for a fibre guiding around 800 nm (from [23]).

current attenuation figures for a conventional index-guiding fibre (0.15 dB km^{-1} by Sumitomo Electric Ltd) and solid core PCF (0.18 dB km^{-1} by NTT Comm.). Nevertheless, the lowest loss reported to date for the state-of-the-art HC-PCF (based on the honeycomb structure with a high air-filling fraction cladding) stands at 1.2 dB km^{-1} [27] for a fibre with a PBG centred at 1550 nm (figure 3(E)). This is an order of magnitude higher than the potential 0.13 dB km^{-1} predicted theoretically in the same paper. This discrepancy is caused by engineering limitations when fabricating the fibre. Indeed, although the confinement loss of the fundamental mode is mainly suppressed by adding eight layers of holes or more to the photonic crystal cladding, additional loss is caused by the coupling from the fundamental mode to other high attenuation modes induced by the surface roughness that arises from thermally excited surface capillary waves frozen in the fibre during the fabrication process when the glass solidifies [28, 29].

The typical chromatic dispersion of a PBG HC-PCF has a characteristic S-shape with an average value within the bandgap <100 ps nm^{-1} km^{-1} (figure 3(D)) and a zero-dispersion wavelength that can be found within the bandgap. This zero-dispersion point can be designed to suit a particular nonlinear process. Similarly, the polarization properties of the fibres can be tailored by designing the core defect so it becomes birefringent [30, 31]. Although such tailoring can affect the attenuation of the fibre, the outstanding properties offered by the HC-PCF far outweigh this drawback, as demonstrated by Gérôme *et al* [32] where the control of the zero-dispersion point leads to unprecedented soliton propagation. An additional benefit of these fibres is their high resilience to bending, meaning that light trapping could still be achieved if the fibre is enclosed in a compact package.

But one of the optical characteristics intrinsic to the mechanism of PBG guidance can cause major problems for the generation and propagation of ultra-broadband frequency combs. Although the fibre effectively traps light in a micrometre-scale core for potentially kilometres, the bandwidth over which the fibre guides is restricted by the extent of the PBG. In addition to this limitation, a further

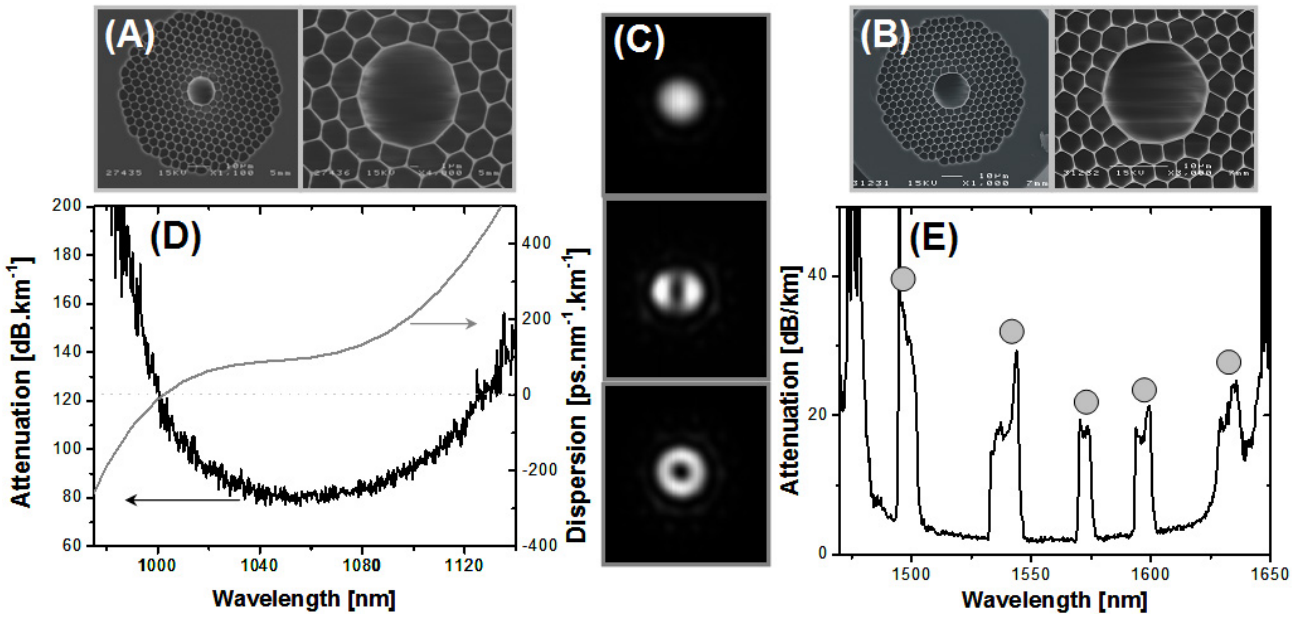

Figure 3. ((A), (B)) Scanning electron micrographs of the state-of-the-art of the seven-cells' defect core and nineteen-cells' defect core photonic bandgap fibre, respectively. (C) Experimental observation of the (top) HE_{11} fundamental core mode and (bottom) other higher-order modes in a seven-cells' defect core fibre guiding at 1550 nm. Optical characteristics: (D) attenuation (black line) and chromatic dispersion (grey line) of seven-cells' defect core fibre. (E) Attenuation of a nineteen-cells' defect core fibre with a loss of 1.2 dB km^{-1} with a bandwidth limited by anti-crossing events, indicated as grey dots and creating high loss peaks.

constraint is imposed by the interaction of the air-guided modes with surface modes, at the interface between the photonic crystal cladding and the core defect, that have some degree of symmetry and spatial overlap (figure 4) [26, 33]. This interaction causes an 'anti-crossing' between the two modes in the DOPS diagram, where their respective dispersion curves repel each other. This anti-crossing leads to a dramatic increase in the transfer of energy from the core mode to the high attenuation surface mode and creates high attenuation regions at the frequency of these anti-crossings that further reduce the operational bandwidth and affect the overall transmission of the HC-PCF (see figure 3(E)). The position of these anti-crossings can, however, be managed by controlling the shape of the core so that they occur near the edges of the transmission spectrum as was shown theoretically by Amezcua-Correa *et al* [34]. Based on these results, an HC-PCF with a 50% core thickness and with no measurable surface modes within the main bandgap was demonstrated experimentally [35]. Later, Wang *et al* [36] presented a series of systematic measurements on a single fibre with a core thickness controlled using an etching method, corroborating the results found in [34].

The attenuation related to confinement and surface roughness will increase for HC-PCF designed to guide at visible and UV wavelengths. Indeed, in these fibres, the cladding structure is scaled down so that PBG guidance occurs at shorter wavelength. As a result, the light-in-air fraction of the air-guided modes is reduced and hence, the total fibre attenuation increased to several dB m^{-1} (figure 5). Also, the difficulty arising from fabricating UV- and visible-guiding fibres with small pitches (<2 μm) and thin structures (air-filling fraction $>90\%$) means that the available bandwidth of such a fibre is often reduced.

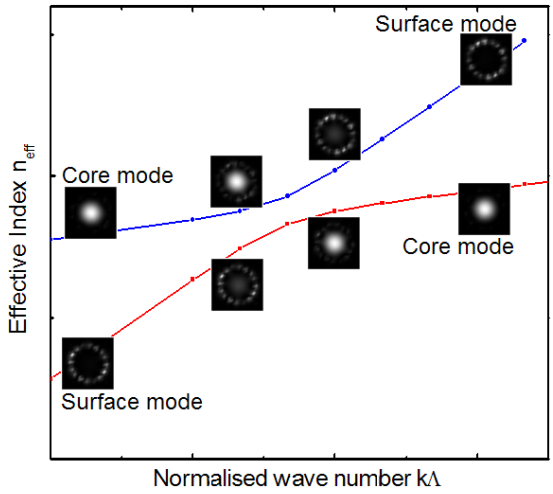

Figure 4. Example of trajectories of the fundamental core mode and a surface mode in the $\{k\Lambda, n_{\text{eff}}\}$ plane as they interact around an anti-crossing event; a large energy exchange is observed at the point of anti-crossing, leading to a peak in the attenuation spectrum.

Demonstrations of nonlinear and quantum effects taking advantage of the high efficiency achieved in HC-PCF have boomed over the past decade but have so far been limited to the near-IR [10–18]. The high attenuation and limited bandwidth offered by these fibres in the visible and UV spectral range have so far restricted their implementation to a large number of short wavelength or broadband applications. But another type of HC-PCF holds the potential to solve this setback.

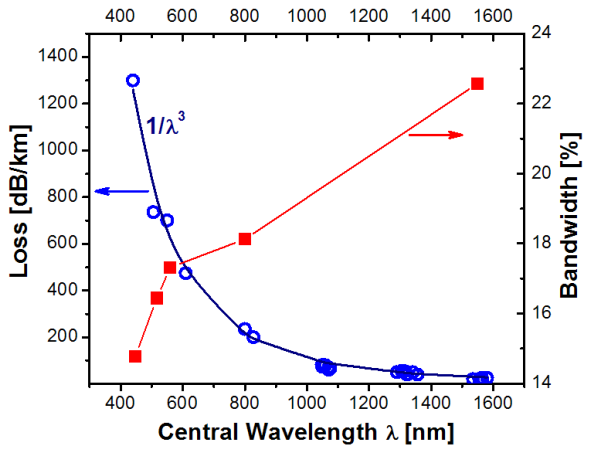

Figure 5. Fibre attenuation (blue circles) and operating bandwidth (red squares) of fabricated HC-PCF as a function of their central operating wavelength. The loss follows a $1/\lambda^3$ evolution (dark blue) instead of the usual Rayleigh scattering ($1/\lambda^4$) [27]. The increase in loss in the visible and UV region of the optical spectrum is accompanied by a reduction in bandwidth.

2.3. An exception to the rule: ultra-broad guidance in large pitch HC-PCF

One can see from the above that low loss air-core guidance is strongly correlated to the absence of photonic states in the photonic crystal cladding. This correlation, however, seems to fall apart for HC-PCF with large pitch (i.e. operating at high frequencies $k\Lambda > 50$). Initially investigated as a possible candidate for photonic bandgap guidance, these fibres were experimentally observed to guide light over an extremely broad optical wavelength range with low attenuation relative to a silica capillary, even when the cladding's air-filling fraction is well below 90% [10]. This property generated great interest for efficient broadband nonlinear effects, even though at the time the guidance mechanism was not understood. As a matter of fact, it was found that, although these fibres do not exhibit any PBG that would trap light over such a frequency span, their guidance is somewhat related to regions of low density of photonic states calculated for such high $k\Lambda$ (figures 6(C) and (D)) [37]. However, this observation does not in itself explain such broadband guidance as one would expect the presence of photonic states in the structure, however small, to cause mode hybridization between the hollow core mode and the cladding modes, in the same way as the air-guided mode of a PBG HC-PCF interacts with the continuum of cladding modes at the boundaries of the PBG to increase its optical attenuation.

A revived interest in this type of fibre came from experimental works on the guidance properties of large pitch HC-PCFs with cladding structures such as the Kagomé design (based on a tessellated Star of David pattern) initially investigated by Benabid *et al* [10], a triangular lattice similar to that used for PBG fibres and a square lattice, reported in both silica [38–40] and polymer [41, 42]. These results not only provided further evidence of the strength of this guidance mechanism, but also provided clues on the mechanism behind it. As was first pointed out in [37], the low density of states observed within the guided optical range gives rise to core modes strongly confined in the hollow core. A direct embodiment of this observation is that the calculated overlap integral between the air-guided core mode and the cladding modes becomes very low at these frequencies [41] (figures 6(C) and (D) inset). An attempt at better explaining such an optical behaviour was made by drawing a parallel between Kagomé fibres and Bragg fibres [43] through an approximated approach that successfully identified the position of the non-guiding spectral bands of the Kagomé structure. It was later suggested that the guidance emerges from the washing-out of the overlap of the core and cladding modes due to a strong transverse-field mismatch between the fast phase oscillations observed within the 'glassy' cladding-field component and the slowly varying core-field distribution [44]. This inhibited coupling is observed even for cladding modes of the same symmetry class as a core mode and with effective index values which differ by only $\Delta n \sim 10^{-5}$ or less from the core mode index. This coexistence of 'bound' states (core modes) within a continuum (cladding modes) has been linked to the Von Neumann–Wigner bound states of quantum electronics [45].

From this new concept, it was found that a low attenuation could be achieved by reducing the overlap between air-guided and cladding modes. Practically, this is done by minimizing the number of glass nodes that appears at the intersection of the struts in the fibre cladding and the strut thickness relative to the air hole diameter [40] and maximizing the air hole diameter with regard to the free-space wavelength. The narrow resonances corresponding to strong anti-crossing events between glass strut modes and air hole modes within the photonic structure (see figures (C) and (D)) and hence high attenuation in the optical spectrum, can also be controlled via thinning of the struts [44].

This new generation of HC-PCF enables low optical attenuation over an ultra-broad bandwidth spanning the UV and the visible part of the spectrum and, in that respect, is complementary to the PBG HC-PCF that has lower attenuation in the near-IR. Figures 7(A) and (B) shows the transmission spectrum for a single Kagomé lattice fibre and a single cell square lattice fibre. Both fibres exhibit spectrally flat regions of high transmission spanning the visible and the near-IR. The typical loss is of the order of 1 dB m^{-1} in the IR and below 2 dB m^{-1} around the visible wavelength for both fibres. The latter value is above that of the photonic bandgap HC-PCF guiding in the same spectral range, though it offers a much larger transmission bandwidth. It was also suggested theoretically in [44] that the attenuation in the UV and visible regions of the spectrum could fall below 100 dB km^{-1} in a specially designed square lattice fibre.

Whilst the large pitch fibre offers a much larger light-in-core fraction than their PBG counterparts, their core diameter is, by design, larger than the equivalent PBG fibre's air core. A large pitch fibre core defect created by removing a single cell (figure 6(A)) has a similar size to a nineteen-cell defect core in a PBG fibre (figure 3(B)). As a result, one would think that a large amount of high-order modes can be accommodated in the core, in addition to the fundamental mode. Their loss, however,

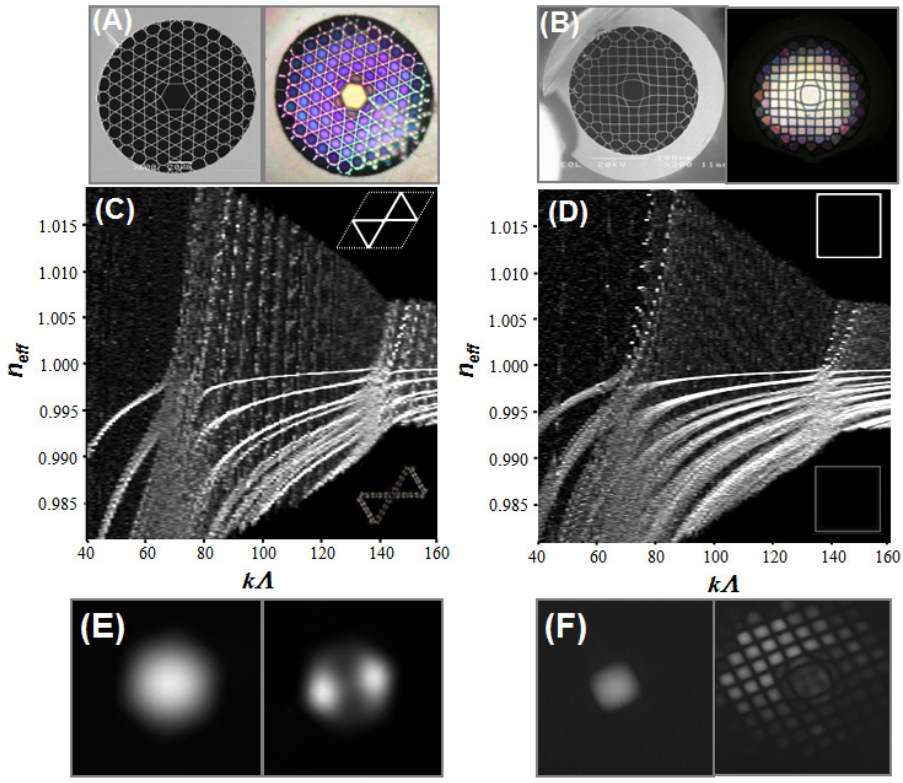

Figure 6. ((A), (B)) Scanning electron and optical micrographs of silica-based large pitch Kagomé lattice and square lattice fibres, respectively. ((C), (D)) Density of photonic states plot for Kagomé lattice and square lattice structures, respectively, with the same strut thickness and similar node size. Inset: (top) unit cell and (bottom) example of a cladding mode showing their high light-in-glass fraction and their fast phase oscillation for Kagomé and square lattice, respectively. (E) Experimental observation of the HE_{11} fundamental mode and higher-order mode propagating through Kagomé fibre. (F) Experimental near-field profile at the output of the square lattice when the input light is coupled to (left) the core or (right) the cladding of the fibre (from [38] and [40]).

is significantly higher than for the fundamental core mode since they strongly interact with cladding modes of matching effective index. Experimentally, only the low attenuation modes are therefore observed; for example, in the case of a single-cell defect core Kagomé fibre, only the fundamental mode and two of the fourfold-degenerate higher-order modes can be coupled into (figure 6(E)). Finally, because of the fast oscillating phase of the silica modes that exist in the guidance band, this fibre does exhibit, similarly to PBG HC-PCF, a high degree of resilience to bend loss [44].

Thanks to the large size of the core defect and to the low light-in-glass fraction of the air-guided mode, the fibre exhibits a low birefringence and a limited bend loss within the band of guidance [40]. More importantly, the flat broadband transmission observed in these fibres is accompanied by low group velocity dispersion, making the fibres ideal candidates for the generation of Raman sidebands or other broadband nonlinear effects where the gain is affected by chromatic dispersion of the propagating medium. Figure 7(C) presents the chromatic dispersion of the fundamental mode of a square lattice single-cell defect fibre. The dispersion has the typical tilted, flattened S-shape of a photonic bandgap fibre, though the average figure throughout the whole transmission region is below 1 ps nm^{-1} km^{-1}, matching that of a silica capillary of similar core diameter and well below that of a PBG HC-PCF.

2.4. Compact photonic microcells

In order to harness the full potential offered by the high gas–laser efficiency achieved in these HC-PCF and to realize highly efficient Raman devices, techniques for filling the fibre with an active gas and hermetically splicing it to conventional fibre have been developed to create a compact, easy-to-use all-fibre solution [5]. An example of such a 'photonic microcell' is shown in figure 8, along with the key steps of the fabrication process for high pressure gas cells. Typical splice losses below 1 dB have been reported for fibres guiding around 1550 nm using a filament fusion splicer.

Such devices enable extreme nonlinearities in a compact all-fibre system and are used in the following sections for ultra-efficient Raman scattering and the generation of ultra-short pulses in a portable solution. Concurrent efforts were also directed towards designing microcells that can accommodate vacuum pressure gases to achieve pressure-limited quantum optical effects such as electromagnetically induced transparency [46].

3. Stimulated Raman scattering in photonic microcells

Stimulated Raman scattering (SRS) is the two-photon inelastic scattering of an incident laser beam by the molecular excitation

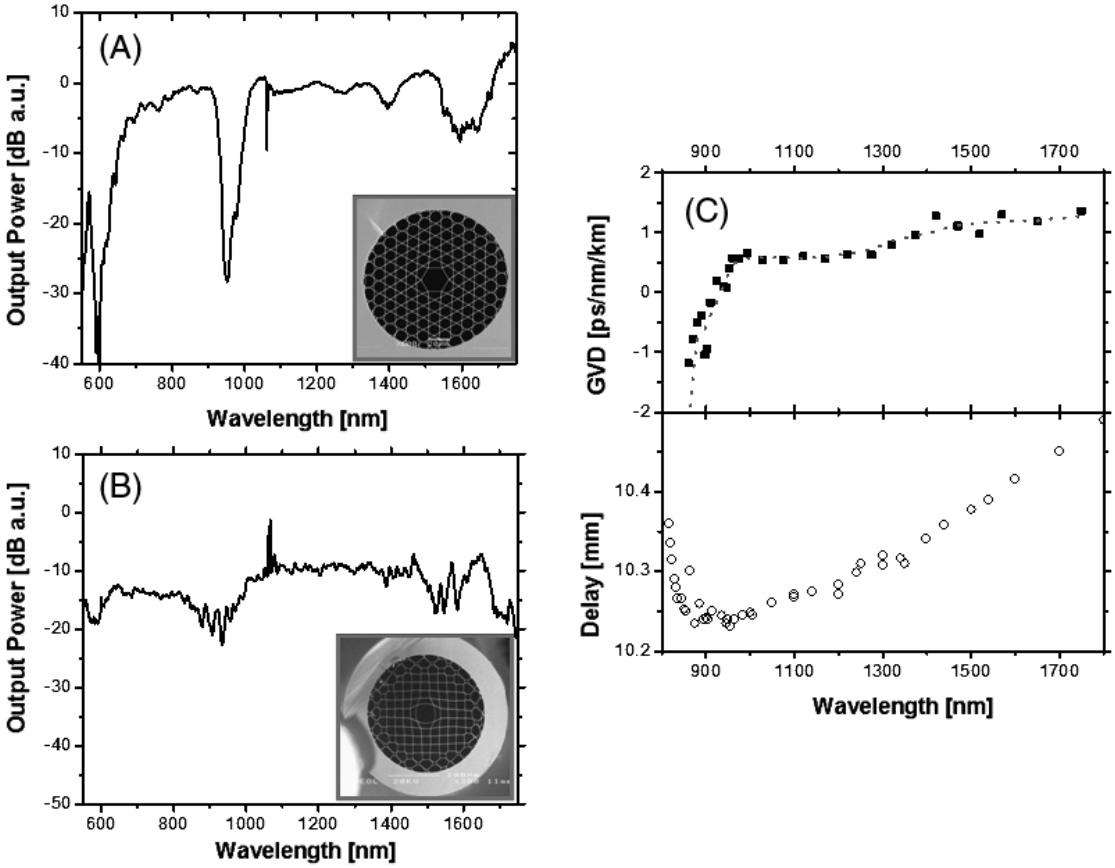

Figure 7. ((A), (B)) Transmission spectrum for silica-based Kagomé and square lattice fibre, respectively. (C) Experimental measurement of (top) chromatic dispersion and (bottom) group delay through 1 m of square lattice fibre as a function of wavelength (from [40] and [44]).

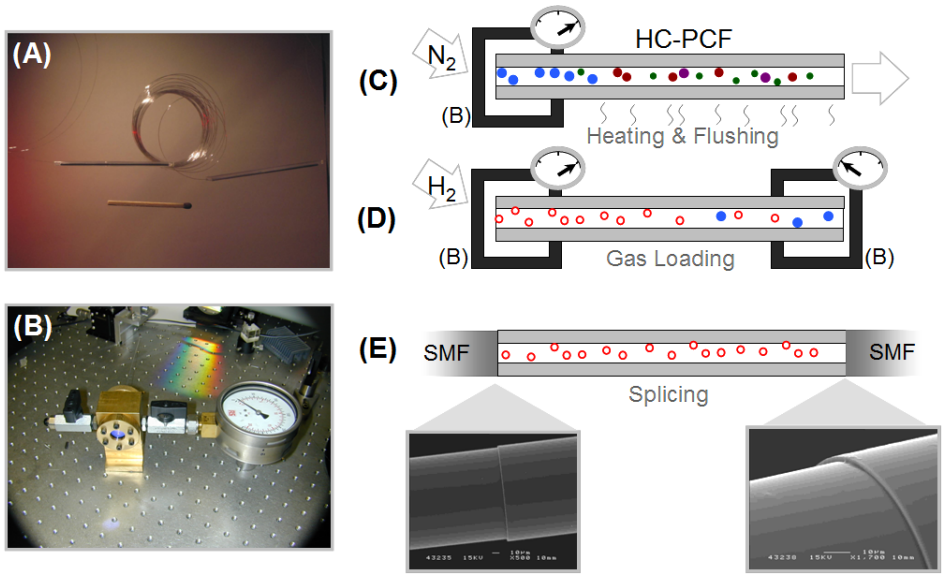

Figure 8. (A) Photonic microcell compared to a matchstick. The two metallic wires attached to the fibre are splice protectors. (B) Brass gas control chamber for loading of high pressure gas. ((C)–(E)) Key steps in the preparation of high pressure gas cells: (C) heating and N_2 flushing for removal of impurities and water, (D) gas loading process by differential pressure, (E) splicing of the high pressure gas-filled HC-PCF to conventional fibre. Insets: scanning electron micrographs of splices.

of the Raman medium, resulting in a frequency down-converted (Stokes line) or up-converted (anti-Stokes line) photon shifted from the pump frequency by the Raman transition frequency Ω_R [47, 48]. The output intensity I_S at the converted Stokes frequency grows exponentially from the incident Stokes power I_{S0}. In the steady state regime, the

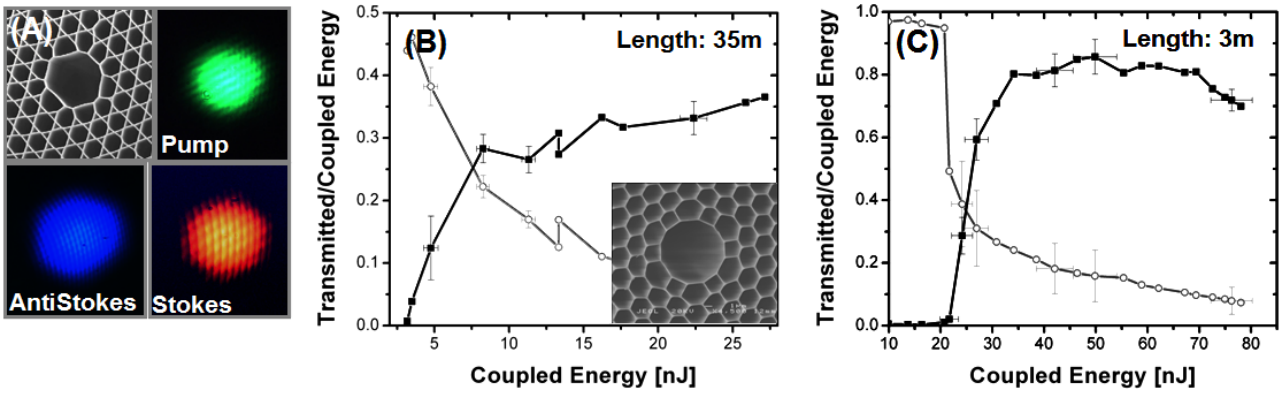

Figure 9. (A) First observation of stimulated Raman scattering in HC-PCF filled with H_2, obtained in (top) a Kagomé lattice fibre coupled to a laser pump at 532 nm. (Bottom) Both vibrational Stokes and anti-Stokes are observed. ((B), (C)) Evolution of the ratio of transmitted average power over the coupled power as a function of the coupled pump power for the pump laser (grey line and circles) and the generated rotational Stokes (black line and squares) through (B) 35 m and (C) 3 m of photonic bandgap fibre filled with H_2 (from [10] and [11]).

amplification follows the simple expression $I_S \sim I_{S0} \exp[gz]$, where gz is the Raman net gain. This highly efficient frequency conversion process is now a familiar phenomenon, used for a wealth of applications, including Raman gas lasers [8, 9], high-resolution spectroscopy [49] or Raman microscopy [50].

This process greatly benefits from the HC-PCF technology, whereby extremely high Raman net gain gz can be obtained with moderate laser power P_{pump} and increased conversion efficiency, thanks to their micrometre-scale effective area A_{eff} and ultra-long interaction length z:

$$gz = \frac{g_{SS} P_{\text{pump}} z}{A_{\text{eff}}} \tag{2}$$

with g_{SS} the steady state Raman gain coefficient of the material expressed generally in cm GW^{-1}. For example, a 1 W CW laser propagating through 10 m of HC-PCF with a core diameter of 10 μm could provide the same Raman net gain as a 10 kW laser propagating in a capillary configuration (10 cm long, 100 μm bore radius). Furthermore, extremely high gain ($G > 100$) can then be achieved with a peak power of less than 1 kW. In such a high net gain configuration, the Stokes field can be seeded from quantum noise, allowing efficient Raman amplification to be achieved in single pump laser configurations. Furthermore, and as will be discussed in section 3.3, the unusually long interaction length z of the fibre enables new excitation conditions for Raman amplification, ideal for generating broadband coherent frequency combs.

3.1. Early results on SRS in HC-PCF

The original demonstration of stimulated Raman scattering in gas-filled HC-PCF was reported by Benabid *et al* [10] and consisted of the observation of the pure vibrational transition $Q_{01}(1)$ first-order Stokes and anti-Stokes lines in a H_2-filled Kagomé lattice fibre by use of a nanosecond pulsed frequency-doubled Nd:YAG laser (figure 9(A)). Despite the high attenuation of the fibre used in this work when compared with today's state-of-the-art hollow core fibre, the general threshold of the effect was dramatically reduced compared to previously reported methods (e.g. [51]).

The advent of the low loss photonic bandgap HC-PCF meant that Raman amplification in the fibre could be achieved at an even lower power threshold and with improved conversion efficiency. By taking advantage of the limited bandwidth offered by the PBG, it also became possible to selectively obtain high conversion efficiency into pure rotational Stokes lines $S_{00}(1)$ of *ortho*-hydrogen, spaced by 17.6 THz instead of the 125 THz of the vibrational lines. In an experiment by Benabid *et al* [11], a seven-cell defect core photonic bandgap fibre with a bandwidth centred at 1060 nm was filled with 7 bar H_2 and coupled to a passively Q-switched Nd:YAG diode pumped solid state laser. Figures 9(B) and (C) present the transmitted power as a function of the coupled energy at the pump and Stokes frequencies for a long (35 m) and a short (3 m) piece of HC-PCF. A 92% conversion efficiency was observed through the short piece of HCPCF, the highest conversion value reported for SRS to date, whilst the long piece of HC-PCF provided a lower threshold for Raman emission of only ~3 nJ, a value 10^6 times lower than reported with conventional techniques [52–54]. This experiment demonstrated for the first time the true potential of HC-PCF as a Raman converter for compact and efficient Raman scattering experiments using low power lasers.

3.2. An integrated Raman photonic microcell

The success of the initial Raman experiments was greatly helped by the design of gas control chambers to achieve the correct gas-filling process whilst allowing optical coupling to the fibre via quartz anti-reflection-coated windows (figure 8(B)). The advent of low loss hollow core splices, in parallel with the development of yet even lower attenuation fibres, meant that an all-fibre integrated photonic microcell filled with high pressure H_2 and spliced to conventional fibre with low loss could yield unprecedented Raman conversion. Such a compact gas cell was reported by Benabid *et al* [5], together with a vacuum pressure microcell filled with acetylene and aimed at laser frequency locking. Figure 10(A) shows the reported Raman spectra at 200 W peak power using a 1047 nm Q-switched Nd:YVO_4 pump laser coupled through the H_2 gas

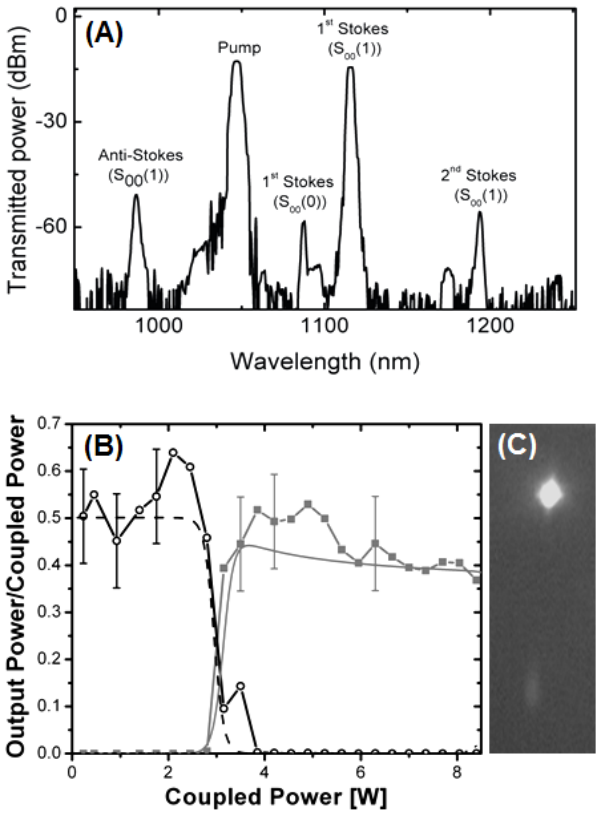

Figure 10. (A) Example of the optical spectrum at the output of a photonic microcell, showing several rotational Raman lines limited by the bandgap bandwidth. (B) Experimental demonstration of continuous-wave Raman conversion with 99.99% of output power at the Stokes wavelength in a single-pass configuration. (C) Observation of the dispersed output spectrum for the (top) Stokes and pump (bottom) wavelength (from [5] and [55]).

cell made up of 5 m of HC-PCF guiding around 1064 nm and spliced to SMF28 with <2 dB per splice. The richness of the generated spectrum at such low peak powers illustrates the extreme effectiveness of the gas cell as a Raman converter. Indeed, at this power level, the stimulated Raman scattering-generated spectrum comprises, in addition to the first Stokes line $S_{00}(1)$ at 1115 nm, a second Stokes (1192 nm) and first anti-Stokes (986 nm). This process is, however, spectrally limited by the PBG guidance and only covers a maximum of 70 THz. This restriction in the number of Stokes components generated hints towards the use of hollow core fibres with larger spectral bandwidth, such as the large pitch HC-PCF, for the generation of broader frequency combs.

Another conclusion that sprang from the initial experiments reported by Benabid *et al* [11] was that the Raman threshold achieved in HC-PCF was so low that efficient Raman conversion could potentially be achieved in the CW regime. As high power narrow-linewidth CW fibre lasers became commercially available, the first single-frequency, CW pure rotational Raman laser based on H_2-filled HC-PCF was realized [55] (figures 10(B) and (C)). The device exhibited up to 99.99% of the output power at the first Stokes radiation, even at a pressure as low as 1 bar, with 50% quantum conversion efficiency of the coupled pump power, and a narrow linewidth. It was also demonstrated that the observed coupled pump power threshold could be reduced to below 1 W by the use of fibre Bragg gratings to form a cavity. Using this arrangement, a dual-wavelength laser source, spaced in frequency by the Raman transition frequency, could potentially be obtained at any wavelength.

3.3. Control of the regimes of Raman amplification

The high net Raman gain gz achieved in HC-PCF improves dramatically the Raman amplification process, both in terms of threshold and conversion efficiency. However, a less obvious advantage to using HC-PCF resides within the Raman mechanism itself, and more specifically, the various regimes of Raman amplification.

When considering such a high gain system in a single pump configuration, it is important to treat the Raman problem within the quantum mechanics framework [56]. For a one-dimensional propagation, Raman amplification can then be cast by the Maxwell–Bloch equations within the Heisenberg representation [57]:

$$\frac{\partial \hat{E}_S}{\partial z} + \frac{1}{c}\frac{\partial \hat{E}_S}{\partial t} = -i\kappa_2 \hat{Q}^* E_L \tag{3a}$$

$$\frac{\partial \hat{Q}^*}{\partial t} = i\kappa_1 E_L^* \hat{E}_S - \Gamma \hat{Q}^* + \hat{F} \tag{3b}$$

linking the (forward propagating) electric field for the continuum of radiation modes near the Stokes transition frequency, represented by the operator $\hat{E}_S$ and the non-depleted laser field amplitude E_L to the collective atomic operator $\hat{Q}$ that represent the slowly varying nuclear coordinate of the ensemble of molecules in the Raman medium. Equation (3*b*) also includes the damping of these molecular oscillations due to collisions at the dephasing rate Γ. More importantly, and contrary to a semiclassical treatment of the problem, this quantum framework allows the inclusion of quantum noise via the Langevin operator $\hat{F}$, whilst maintaining the commutation relations in the operator $\hat{Q}$. From these quantum fluctuations arise spontaneous photons at the Stokes frequency that can effectively seed the stimulated Raman process. The coupled constant κ_1 and κ_2 depend on the molecular polarizability of the medium and are linked to the Raman gain g_{SS} of the medium defined by

$$g_{SS} = \frac{2\kappa_1\kappa_2}{\Gamma} E_L^2. \tag{4}$$

Exact solutions to the coupled equations (3), in the case of a single pump configuration and where the initial Stokes intensity arises from quantum noise fluctuations I_S^{noise}, were reported in the early 1980s by Raymer and Mostowski [57]. The interested reader can find further details of this theory and its comparison with the semiclassical approach in [56].

Figure 11 reproduces the calculated solution for the normalized generated Stokes field I_S/I_S^{noise} as a function of normalized time $\Gamma\tau$, where τ is the pump pulse duration and for various values of the Raman net gain gz. One can identify the incoherent spontaneous regime, achieved for pump pulses shorter than a characteristic time given by $\tau_1 = 1/gz\Gamma$, where

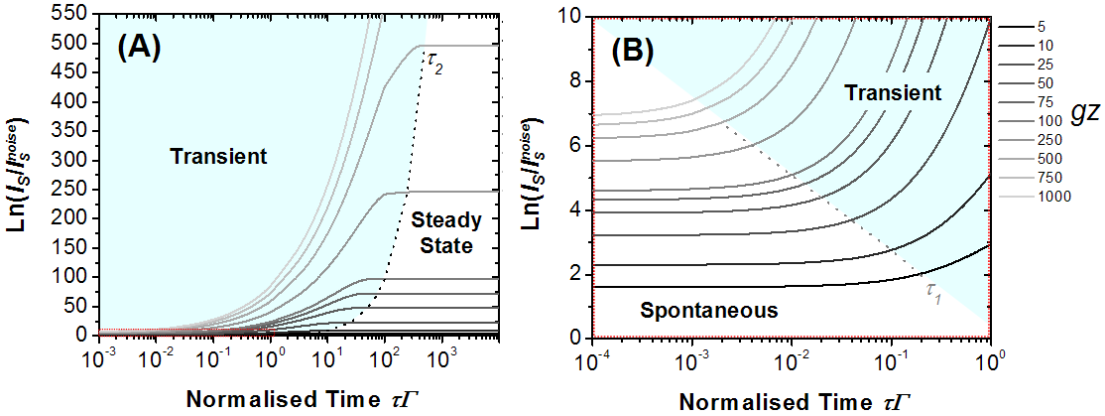

Figure 11. Normalized Stokes intensity growth from quantum noise fluctuation I_S^{noise} as a function of normalized pump laser pulse width $\tau\Gamma$ for different values of gz (spanning from 5 to 1000) for (A) high values and (B) low values of $\ln(I_S/I_S^{noise})$. The transient regime is highlighted as a shaded area. The passage times τ_2 and τ_1 are identified as dotted lines in (A) and (B), respectively.

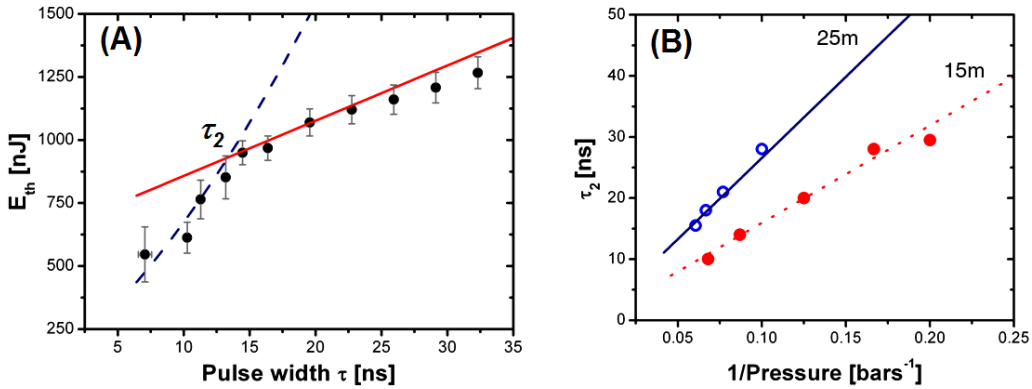

Figure 12. (A) Measured threshold energy E_{th} versus pulse width τ (black circles) for a hydrogen pressure of 11.5 bar and an HC-PCF length of 15 m. The inflection point denotes the passage time τ_2. (B) Experimental τ_2 as a function of the inverse of the H_2 pressure for a fibre length of 15 m (red dots) and 25 m (blue circles). The theoretical evolution $\tau_2 = gz/\Gamma$ is represented by dotted red and solid blue lines, respectively (from [59] and [60]).

the independent scattering of incident photons does not build up to an efficient Stokes emission. For pulses larger than a second characteristic time given by $\tau_2 = gz/\Gamma$, on the other hand, the amplification is in a steady state regime where the Stokes field can be approximated to the familiar form $I_S \sim I_{S0}\exp[gz]$. In this regime, the collisional dephasing rate Γ leads to the loss of phase correlation between the emitted Stokes field and the initial pump field. As a result, an ensemble of Stokes frequencies generated in this regime will not be automatically phase-locked and pulse compression will become impossible.

This state-of-affairs changes, however, for pump pulse durations between the two characteristic times τ_1 and τ_2, where the regime is said to be transient [57]. Indeed, as opposed to the steady state regime when the Stokes intensity is independent of the pump pulse duration, the transient Stokes intensity strongly depends on τ and grows as $\sim\exp[\sqrt{8gz\Gamma\tau}]$, leading to a Stokes pulse of duration $\tau_S = \sqrt{\tau/16gz\Gamma}$ [58] which can be much shorter than the dephasing time $T_2 = 1/2\Gamma$. As a result, the Stokes field generated in the transient regime of Raman amplification is expected to retain a high degree of molecular coherence with the initial pump field.

Thanks to the linear dependence of the transient passage time τ_2 with the Raman net gain gz, the use of HC-PCF lifts the restriction that pump laser pulse duration needs to be smaller than the dephasing time T_2 to achieve efficient transient amplification. This was confirmed experimentally by observing the transient amplification of rotational Stokes $S_{00}(1)$ that grows efficiently from quantum noise fluctuations for pump laser pulses τ longer than 10 ns [59, 60] (figure 12(A)). As a matter of fact, this transient passage time τ_2 can be accurately controlled (figure 12(B)) via a wise choice of fibre length and gas pressure such that ultra-long pulses could be used in the transient regime of Raman amplification for the generation of phase-locked optical frequency combs.

4. Multi-octave frequency comb generation in large pitch HC-PCF

The most promising alternative to high harmonic generation for the creation of attosecond pulses is the technique based on Raman sidebands by adiabatically driving the Raman medium to maximum molecular coherence. This technique, first suggested and demonstrated by Harris and

co-workers [3, 4], achieves high conversion efficiency and an ultra-broad spectrum consisting of a large number of mutually phase-locked high-order Stokes and anti-Stokes fields over a very large frequency span. The technique has now been further refined by using capillaries [61] or a high finesse cavity [62] to increase the gas–laser interaction length. The coherence and the broadband nature of the sideband spectrum mean that it should be possible to synthesize sub-femtosecond optical pulses. However, it has been argued qualitatively that one could obtain a similar coherent high-order stimulated Raman scattering spectrum using a single pump laser, provided one operates in the transient and high gain regime of Raman amplification [63–65]. So far, this requirement meant the frequency comb was only generated using GW-power, transform-limited sub-picosecond lasers, but the preliminary results presented above indicate that the highly coherent transient regime of rotational SRS could be extended to low power nanosecond pulses by use of an HC-PCF. Nevertheless, a photonic bandgap HC-PCF would hinder the number of generated frequency components, due to its modest ∼70 THz available bandwidth. This is far away from the ∼1000 THz bandwidth required to generate attosecond pulses in the IR–UV domain.

The ultra-broad bandwidth achieved in large pitch HC-PCF lifts these limitations by offering a transmission spectrum spanning from UV to mid-IR with low dispersion, low loss and a high-quality mode profile. This final section presents the realization of a gas cell based on such a fibre and its use for the generation and guidance of a higher-order stimulated Raman scattering comb-like spectrum spanning three optical frequency octaves and including up to 45 high-order Stokes and anti-Stokes components. The comb is generated by coherently exciting the confined gas in the transient regime of Raman amplification with a single, moderately powerful infrared nanosecond pulsed laser. The system achieves maximum molecular coherence of the Raman-active gas at room temperature and cuts the required laser power for efficient conversion by six orders of magnitude compared to current Raman sideband generation techniques, offering a robust, inexpensive and straightforward way of finding viable alternatives to high harmonic generation in synthesizing attosecond pulses.

4.1. Mechanism of frequency comb generation in HC-PCF

As demonstrated by Benabid *et al* [59], the HC-PCF offers the possibility to extend the transient regime of Raman amplification to pulse lengths much longer than T_2 and with a peak-power level lower than experiments in free space or using silica capillaries. For example, by using 1 m of single-cell defect core Kagomé lattice fibre (with ∼20 μm core diameter), one could use pulses as long as 700 times T_2 with peak powers as low as 10 kW, whilst remaining in the transient regime of amplification, creating a new and favourable situation for the generation of coherent SRS for pulses >10 ns. Indeed, the extension of the pump pulses to much longer durations would enhance the still-transient Raman gain and would weaken the damaging effect of group velocity dispersion in the generation process.

The broadband low loss light guiding and confining features of the large pitch HC-PCF means that a single pump laser configuration can be used for the Raman amplification and Stokes/anti-Stokes comb generation over a frequency span approaching that of the 1000 THz required for attosecond pulse generation. This system also offers flexibility over the choice of Raman medium used and the pump wavelength, lifting the limitation of the Raman sideband technique, restricted to using deuterium as the Raman medium and to Nd:YAG and Ti:sapphire lasers due to the high laser power necessary to achieve efficient conversion.

The key question that needs to be addressed with regard to attosecond pulse generation is the mutual phase relationship between the comb components generated along the fibre. Indeed, due to the random nature of the spontaneously initiated Stokes emission, the mutual phase coherence of the Stokes and anti-Stokes lines may not be achieved. However, the quantum analysis of a similar problem using broadband multi-line pump lasers [57, 66] showed that automatic phase coherence with the pump could be achieved, even though the Stokes was initiated by spontaneous emission. These results corroborated those obtained earlier by Carman *et al* [67] using the classical approach. In order to deal with the present case of a single-frequency pump and several Stokes and anti-Stokes (S/AS) lines, a new quantum analysis is required. This analysis was reported in [45] and stems from previous work which, however, was limited to either the Stokes amplification [68] or to the anti-Stokes one [69]. Qualitatively, one could describe the newly developed theory in a more familiar picture of parametric processes whereby the Stokes is amplified from spontaneous emission in the transient regime followed by four-wave mixing to produce all subsequent Raman sidebands.

The quantitative derivation of this new analysis, applied to an isolated vibrational (or rotational) Raman transition, consists of solving the coupled equations of motion in a similar manner to equations (3) but with the field being extended to the pump and an arbitrary number of Stokes/anti-Stokes pairs. This is done in a non-perturbative iterative approach whereby the equation of motion for the first-order pair of Stokes/anti-Stokes are solved following the method developed by Kilin [69]. It becomes apparent that the initial noise field, corresponding to a thermal distribution of the temporal–spatial modes of the molecular vibration (or rotation), is filtered out under the narrow band, high net gain condition to yield a Stokes and anti-Stokes field determined solely by the dominant temporal–spatial mode, which corresponds to the highest Raman gain. It is also found that the generated Stokes and anti-Stokes are anti-correlated with a deterministic (i.e. a degree of correlation close to 1) phase whose value is random from laser shot to shot, indicating that the phases of these two fields is automatically locked for each pulse.

The second step of the theoretical method consists of iteratively extending the above treatment to higher-order sideband pairs. By writing the coupled equations for the generation of the second pair of Stokes/anti-Stokes pairs, one finds that their growth is governed by the first Stokes/anti-Stokes pair acting as a pump source, in such a way that the phase of the second pair of sidebands is deterministically

related to that of the first pair. The results of this iterative process shows that all higher-order Stokes/anti-Stokes pairs retain the same key features of sharing a common phase related to that of the first pair, hence creating an ideal scenario for the generation of sub-femtosecond pulse trains.

In analogy with the generation of Raman sidebands in the adiabatic regime [3], those results can be viewed as the generation of a coherent molecular spatial excitation, which modulates the first Stokes/anti-Stokes pair by adding sidebands. In turn, these sidebands then get modulated to generate sidebands of their own, and so on. The difference between the methods lies in the spontaneous generation of the first Stokes field which means that, in the present case, the overall phase of the generated Stokes fields fluctuates randomly from shot to shot. It is worth noting that a soliton treatment of the Raman sideband problem was reported by Kaplan [70] and could potentially benefit the study of high-order SRS in HC-PCF.

4.2. High-order Raman in Kagomé lattice HC-PCF

Figure 13 shows a schematic diagram of the HSRS experimental set-up as reported in [44]. A 40 cm long sample of Kagomé fibre is filled with H_2 at a pressure of 20 bar and coupled to a single Nd:YAG laser operating at 1064 nm, which generates 12 ns long pulses at 50 Hz repetition rate, with a linewidth ∼40 MHz. As the large-pitch HC-PCF supports cladding modes as well as the air-guided fundamental HE_{11} core mode at the same wavelength, care is taken to couple predominantly to the core. The power and polarization of the laser is controlled by a set of waveplates and a polarizing beamsplitter. Thanks to the polarization dependence of the rotational Raman gain in H_2 [71, 72], the rotational Stokes components of the expected spectrum can be turned 'on or off', whether the polarization is circular or linear, respectively. In order to detect the whole extent of the generated frequency comb, the fibre output beam is collected onto a detection bench where a combination of a multi-channel UV/visible spectrometer (200–800 nm), an optical spectrum analyser (400–1700 nm) and an IR monochromator (1600–3000 nm) are used to create a single spectrum measurement after the three spectrometers have been relatively calibrated.

As the input power is increased above threshold, the comb generation process can be readily observed as green/yellow light escapes from the side of the fibre (figure 14(A)) and bright white light is observed at the output of the fibre (figure 14(B)), indicating a large number of anti-Stokes lines generated in the visible region of the spectrum. Figure 14(E) show the typical transmitted spectrum obtained at 40 kW pump peak power and for a linearly polarized input. In addition to the pump line, the spectrum contains six strong spectral lines consisting of one Stokes (∼1892 nm) and five anti-Stokes components, the fifth anti-Stokes being in the UV (∼332 nm). The lines are equally spaced by ∼125 THz which corresponds to the frequency of the vibrational Raman transition $Q_{01}(1)$ of hydrogen. The spatial-mode images of the observed anti-Stokes spectral lines can be directly observed by using a diffraction grating and projecting the modes onto a screen (figure 14(C)). Due to the variable sensitivity of the camera with wavelength, the strength of the lines is not well reproduced in the picture.

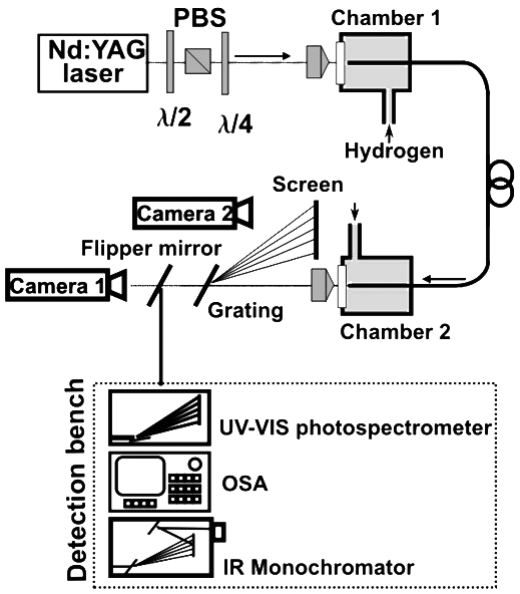

Figure 13. Experimental set-up for the generation of higher-order stimulated Raman scattering. PBS: polarizing beamsplitter, λ/2 : half-waveplate, λ/4 : quarter-waveplate, OSA: optical spectrum analyser (from [44]).

When the laser polarization is changed from linear to circular, the Raman gain of the $S_{00}(1)$ rotational transition is increased above threshold so that each vibrational HSRS components act as a pump for the generation of rotational Stokes and anti-Stokes lines. Overall, a spectrum of 45 spectral components, spaced by 17.6 THz (figures 14(D) and (F)), can be observed, hence covering nearly 1000 THz of bandwidth with a conversion from the pump to the comb of more than 53%. For a time–bandwidth product of 0.4 and if the coherence of the lines is confirmed, such a spectrum could potentially generate trains of ∼500 as pulses spaced by either 125 or 17 THz, depending on the polarization of the input laser. It is also interesting to note that, thanks to the relative low power threshold, no broadening of the spectral linewidth was observed [65].

The present spectra contrast with the previously reported results using high-order SRS in both the impulsive [63] and the transient regimes [64, 65, 73] by possessing higher conversion efficiency into the higher-order Raman lines and a wider spectral span, despite pumping at a longer wavelength [64]. With conversion efficiency from the pump to the comb components comparable to the Raman sidebands technique, the method generates a similar spectral bandwidth with a pump laser peak power almost four orders of magnitude lower and without the constraints imposed by adiabatic preparation. This makes the technique one of the most potentially efficient for frequency comb generation.

4.3. Coherence of Raman lines

In order for the frequency comb observed above to be useful for sub-femtosecond pulse synthesis, all its spectral lines should

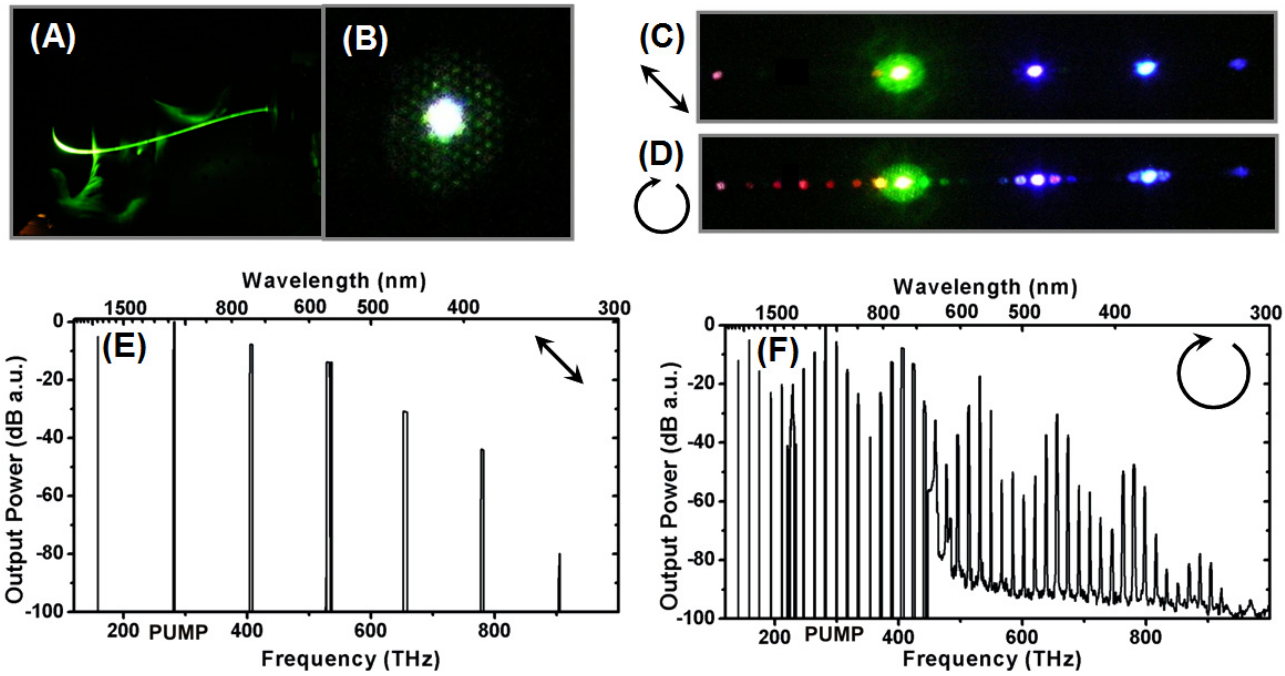

Figure 14. (A) View of the large pitch Kagomé fibre from the side. The laser is coupled into the fibre on the left-hand side of the picture. The fibre output is on the right. The total fibre length is 40 cm. (B) Output end of the fibre, showing a bright white light guided in the core. ((C), (D)) Diffracted output and ((E), (F)) optical spectrum of the generated and transmitted higher-order SRS for a linearly and circularly polarized laser input, respectively (from [44]).

be phase-locked. The theoretical findings of [44], described qualitatively above, indicate that all Stokes and anti-Stokes components of the generated spectrum are mutually coherent, despite their being initiated by spontaneous Raman scattering.

Even though it is difficult to directly measure this phase relationship experimentally, several indications point towards such a high degree of coherence. The observation of high-order transverse modes of the Stokes and anti-Stokes lines propagating through fibre does provide some hints towards a coherent parametric process (figure 15(B)). However, the most striking evidence of the process is provided by plotting the evolution of the output power of the transmitted pump, Stokes and anti-Stokes lines of the vibrational (or ro-vibrational) transition as a function of the input power (figure 15(A)). The simultaneous rise of all three vibrational lines generated above a pump peak power of 13 kW rules out the possible incoherent cascaded SRS process and further confirms the theoretical prediction that all sidebands are coherently generated.

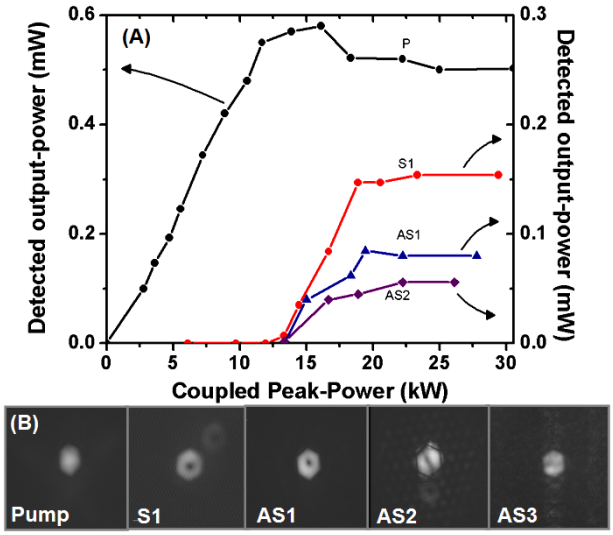

Figure 15. (A) Detected output power taken from a fraction of the output beam diffracted on a grating as a function of the coupled peak power for the pump (black circles and line), first Stokes (red circles and line), first anti-Stokes (blue triangles and line) and second anti-Stokes components (purple diamonds and line). (B) Near-field profile of the output from the H_2-filled Kagomé fibre. The Stokes (S) and anti-Stokes (AS) frequencies are separated from the pump by means of a diffraction grating (from [44]).

5. Conclusion and future work

The enhanced gas–laser interaction offered by the HC-PCF technology has been demonstrated through the realization of compact all-fibre Raman devices. Two types of HC-PCF have been identified as suitable candidates for integration inside these devices: the photonic bandgap HC-PCF offers a low optical loss over a narrow frequency range in the IR region of the optical spectrum, while the large-pitch HC-PCF offers a large transmission bandwidth that covers the UV and visible as well as the near-IR with modest optical transmission. A deeper understanding of the guidance mechanism exclusive to each type of fibre has led to the optimization of their loss and dispersion characteristics for nonlinear applications.

The development of the photonic microcells also benefited from various techniques for loading gas inside HC-PCF and hermetically splicing the fibre to conventional solid core

fibres. The resulting devices exhibited low insertion loss, ease of use and an optimum nonlinear efficiency. Experimental demonstrations of the potential of such devices included a reduction of the power threshold for the observation of the Raman process by a factor of 10^6 compared to previous techniques accompanied by the highest Stokes conversion efficiency reported to date using the pure rotational Raman transition $S_{00}(1)$ in H_2. These results led to the realization, in a single-pass configuration, and using a 'single-pump' laser system, of the first continuous-wave Raman fibre gas laser with near-total conversion of the pump to the Stokes frequency with 50% conversion efficiency.

Crucially, these photonic microcells also provide accurate control over the regime of Raman amplification. Transient Raman operation becomes possible for pump laser pulses much longer than the dephasing time T_2 whilst retaining a high degree of molecular coherence. In this configuration, a frequency comb spanning 1000 THz was generated and guided in a Kagomé-based microcell. Experimental observations and theoretical considerations point towards a relatively high degree of mutual coherence of the spectral components and hint at the possibility of sub-femtosecond pulse generation in a compact, low-budget, all-fibre system.

However, the exact degree of coherence of the spectral components obtained using this method needs to be accurately assessed and the influence of the fibre's chromatic dispersion taken into consideration. Interesting results could spring from using the photonic microcells in the Raman sideband generation technique devised by Harris and co-workers. It could also prove a vital addition to high harmonic generation experiments.

Acknowledgments

The authors would like to thank P S Light, P J Roberts and M G Raymer for co-authoring the demonstration of multi-octave frequency generation in the transient regime of Raman amplification using HC-PCF. The work reported by the authors is funded by the UK Engineering and Physical Science Research Council (EPSRC). FB is an EPSRC Advanced Research Fellow.

References

[1] Hentschel M, Kienberger R, Spielmann C, Reider G A, Milosevic N, Brabec T, Corkum P, Heinzmann U, Drescher M and Krausz F 2001 *Nature* **414** 509
[2] Paul P, Toma E S, Breger P, Mullot G, Augé F, Balcou P, Muller H G and Agostini P 2001 *Science* **292** 1689
[3] Harris S E and Sokolov A V 1997 *Phys. Rev.* A **55** R4019
[4] Sokolov A V, Walker D R, Yavuz D D, Yin G Y and Harris S E 2000 *Phys. Rev. Lett.* **85** 562
[5] Benabid F, Couny F, Knight J C, Birks T A and Russell P St J 2005 *Nature* **434** 488
[6] Agrawal G 2001 *Nonlinear Fibre Optics* (London: Academic)
[7] Renn M J and Pastel R 1998 *J. Vac. Sci. Technol.* B **16** 3859
[8] Brasseur J K, Reparsky K S and Carlsten J L 1998 *Opt. Lett.* **23** 367
[9] Meng L S, Roos P A and Carlsten J L 2002 *Opt. Lett.* **27** 1226
[10] Benabid F, Knight J C, Antonopoulos G and Russell P St J 2002 *Science* **298** 399
[11] Benabid F, Bouwmans G, Knight J C, Russell P St J and Couny F 2004 *Phys. Rev. Lett.* **93** 123903
[12] Ouzounov D G, Ahmad F R, Muller D, Venkataraman N, Gallagher M T, Thomas M G, Silcox J, Koch K W and Gaeta A L 2003 *Science* **301** 1702
[13] Ghosh S, Sharping J, Ouzounov D G and Gaeta A L 2005 *Phys. Rev. Lett.* **94** 093902
[14] Benabid F, Light P S, Couny F and Russell P St J 2005 *Opt. Express* **13** 5694
[15] Thapa R, Knabe K, Faheem M, Naweed A, Weaver O L and Corwin K L 2006 *Opt. Lett.* **31** 2489
[16] Couny F, Light P S, Benabid F and Russell P St J 2006 *Opt. Commun.* **263** 28
[17] Ghosh S, Bhagwat A R, Renshaw C K, Goh S, Gaeta A L and Kirby B J 2006 *Phys. Rev. Lett.* **97** 023603
[18] Light P S, Benabid F, Couny F, Maric M and Luiten A N 2007 *Opt. Lett.* **32** 1323
[19] Russell P St J 2006 *J. Lightwave Technol.* **24** 4729
[20] Maradudin A A and McGurn A R 1994 *J. Mod. Opt.* **41** 275
[21] Birks T A, Roberts P J, Russell P St J, Atkin D M and Shepherd T J 1995 *Electron. Lett.* **31** 1941
[22] Pottage J, Bird D M, Hedley T D, Knight J C, Birks T A, Russell P St J and Roberts P J 2003 *Opt. Express* **11** 2854
[23] Couny F, Benabid F, Roberts P J, Burnett M T and Maier S A 2007 *Opt. Express* **15** 325
[24] Litchinitser N M, Abeeluck A K, Headley C and Eggleton B J 2002 *Opt. Lett.* **27** 1320
[25] Birks T A, Pearce G J and Bird D M 2006 *Opt. Express* **14** 9483
[26] Humbert G, Knight J C, Bouwmans G, Russell P St J, Williams D P, Roberts P J and Mangan B J 2004 *Opt. Express* **12** 1477
[27] Roberts P J *et al* 2005 *Opt. Express* **13** 236
[28] Sanyal M K, Sinha S K, Huang K G and Ocko B M 1991 *Phys. Rev. Lett.* **66** 628
[29] Jäckle J and Kawasaki K 1995 *J. Phys.: Condens. Matter* **7** 4351
[30] Chen X, Li M J, Venkataraman N, Gallagher M, Wood W, Crowley A, Carberry J, Zenteno L and Koch K W 2004 *Opt. Express* **12** 3888
[31] Mangan B J, Lyngsø J K and Roberts P J 2008 *CLEO/QELS:Conf. on Lasers and Electro-Optics/Quantum Electronics and Laser Science (San Jose)* paper JFG4
[32] Gérôme F, Cook K, George A K, Wadsworth W J and Knight J C 2007 *Opt. Express* **15** 7126
[33] Smith C M, Venkataraman N, Gallagher M T, Muller D, West J A, Borrelli N F, Allan D C and Koch K W 2003 *Nature* **424** 657
[34] Amezcua-Correa R, Broderick N G, Petrovich M N, Poletti F and Richardson D J 2006 *Opt. Express* **14** 7974
[35] Amezcua-Correa R, Gèrôme F, Leon-Saval S G, Broderick N G R, Birks T A and Knight J C 2008 *Opt. Express* **16** 1142
[36] Wang Y Y, Light P S and Benabid F 2008 *IEEE Photon. Technol. Lett.* **20** 1018
[37] Hedley T D, Bird D M, Benabid F, Knight J C and Russell P St J 2003 *CLEO/QELS:Conf. on Lasers and Electro-Optics/Quantum Electronics and Laser Science (Baltimore)* paper QTuL4
[38] Couny F, Benabid F and Light P S 2006 *Opt. Lett.* **31** 3574
[39] Beaudou B, Couny F, Benabid F and Roberts P J 2008 *CLEO/QELS:Conf. on Lasers and Electro-Optics/Quantum Electronics and Laser Science (San Jose)* paper JFC6
[40] Couny F, Roberts P J, Birks T A and Benabid F 2008 *Opt. Express* **16** 20626
[41] Argyros A and Pla J 2007 *Opt. Express* **15** 7713
[42] Argyros A, Leon-Saval S G, Pla J and Docherty A 2008 *Opt. Express* **16** 5642
[43] Pearce G J, Wiederhecker G S, Poulton C G, Burger S and Russell P St J 2007 *Opt. Express* **15** 12680

[44] Couny F, Benabid F, Roberts P J, Light P S and Raymer M G 2007 *Science* **318** 1118
[45] Von Neumann J and Wigner E 1929 *Phys. Z.* **30** 465
[46] Light P S, Couny F and Benabid F 2006 *Opt. Lett.* **31** 2538
[47] Shen Y R 2002 *The Principles of Nonlinear Optics* (New York: Wiley)
[48] Boyd R 2000 *Nonlinear Optics* (London: Academic)
[49] Duncan M D, Osterlin P and Byer R L 1981 *Opt. Lett.* **6** 90
[50] Cheng J X and Xie X S 2004 *J. Phys. Chem.* B **108** 827
[51] Guerra V and Kay R B 1993 *J. Phys. B: At. Mol. Opt. Phys.* **26** 3975
[52] Perrone M R, Piccinno V, De Nunzio G and Nassisi V 1997 *IEEE J. Quantum Electron.* **33** 938
[53] De Tomasi F, Diso D, Perrone M R and Protopapa M L 2001 *Phys. Rev.* A **64** 023812
[54] Heeman R J and Godfried H P 1995 *IEEE J. Quantum Electron.* **31** 358
[55] Couny F, Benabid F and Light P S 2007 *Phys. Rev. Lett.* **99** 143903
[56] Raymer M G and Walmsley I A 1990 *Prog. Opt.* **28** 181
[57] Raymer M G and Mostowski J 1981 *Phys. Rev.* A **24** 1980
[58] Raymer M G, Walmsley I A, Mostowski J and Sobolewska B 1985 *Phys. Rev.* A **32** 332
[59] Benabid F, Antonopoulos G, Knight J C and Russell P St J 2005 *Phys. Rev. Lett.* **95** 213903
[60] Couny F, Carraz O and Benabid F 2009 *J. Opt. Soc. Am.* B **26** 1209
[61] Burzo A M, Chugreev A V and Sokolov A V 2006 *Opt. Commun.* **264** 454
[62] Suzuki T, Hirai M and Katsuragawa M 2008 *Phys. Rev. Lett.* **101** 243602
[63] Nazarkin A, Korn G, Wittmann M and Elsaesser T 1999 *Phys. Rev. Lett.* **83** 2560
[64] Kawano H, Hirakawa Y and Imasaka T 1998 *IEEE J. Quantum Electron.* **34** 260
[65] Sali E, Mendham K J, Tisch J W G, Halfmann T and Marangos J P 2004 *Opt. Lett.* **29** 495
[66] Raymer M G and Westling L A 1985 *J. Opt. Soc. Am.* B **2** 1417
[67] Carman R L, Shimizu F, Wang C S and Bloembergen N 1970 *Phys. Rev.* A **2** 60
[68] Raymer M G, Rzazewski K and Mostowski J 1982 *Opt. Lett.* **7** 71
[69] Kilin S Y 1988 *Europhys. Lett.* **5** 419
[70] Kaplan A E 1994 *Phys. Rev. Lett.* **73** 1243
[71] Hermann M R, Chambers D H, Dixit S N and Karr T J 1991 *Phys. Rev.* A **43** 4079
[72] Venkin G V, Il'inskiĭ Y A and Mikheev G M 1985 *Sov. J. Quantum Electron.* **15** 395
[73] Kawano H, Hirakawa Y and Imasaka T 1997 *Appl. Phys.* B **65** 1